Large-eddy simulation of a plane jet in a cross-flow

W. P. Jones and M. Wille
Department of Chemical Engineering and Chemical Technology, Imperial College of Science, Technology and Medicine, London, UK

A plane jet in a cross-flow has been simulated using large-eddy simulation (LES) with artificial inflow and wall boundary conditions. A mesh adapted on the mean velocity field was used to increase the resolution in the jet shear layer. Results from simulations with a standard Smagorinsky–Lilly model, a one-equation model, and a dynamic model are compared. Agreement between the measured and predicted results is reasonable overall, but differences between simulations with the various residual scale models are small.

Keywords: fluid mechanics; turbulence; computation; LES

Introduction

Recently, a number of complex flows have been computed with large-eddy simulation (LES) techniques. The geometries simulated include, for example, backward facing steps (Akselvoll and Moin 1993), flow over a step or a hemisphere (Manhart and Wengle 1993), or flows in duct bends (Breuer and Rodi 1994; Su and Friedrich 1994). The results of these calculations suggest that some of the problems associated with an inadequate representation of the anisotropic and low-Reynolds number turbulence production and dissipation in the near-wall region are relatively insignificant in complex shear flow as compared to flows dominated by wall effects such as turbulent channel and pipe flows.

The difficulties in calculating the flow in the immediate vicinity of the wall must be attributed to the fact that the basic assumption of scale separation fundamental to LES breaks down. As the viscous sublayer is approached, a distinction between the energy containing virtually inviscid motion and the dissipative scales is impossible. (We refer to the region where direct viscous effects are important as the viscous sublayer. Some authors (Tennekes and Lumley 1972) further distinguish between the viscous and the buffer region.) If not all scales associated with the production of turbulent energy are resolved, backscatter from the unresolved to the resolved motion can be observed (Rogallo and Moin 1984), and, as noted in (Härtel and Kleiser 1994), this can become large as the wall is approached. Strictly a *proper LES* calculation of all important scales in the sublayer would effectively correspond to a direct numerical simulation (DNS) of all scales. However, in practice, good results have been obtained for channel and pipe flows at moderate Reynolds number by increasing the resolution just sufficiently to represent the most important structures in the wall region, while at the same time, adjusting the residual scale model by the addition of a wall-damping function (Piomelli 1987) or by using a dynamic model (Germano et al. 1990) to account for the lost turbulence production in the unresolved scales.

For the high Reynolds numbers, Re occurring in engineering practice, the application of such an approach would be prohibitively expensive. If it is assumed that only the largest structures in the viscous sublayer need to be resolved and that the size of these structures scales on the thickness of the viscous sublayer itself, then resolution requirements increase approximately as $\mathrm{Re}^{2.6}$. Here, use has been made of Blasius's law for the friction coefficient in pipe and channel flows to approximate an upper bound for the thickness of the sublayer, $\delta_{\mathrm{sub}} \sim \nu/(u_b\sqrt{\mathrm{Re}^{-0.2}})$, where u_b is the bulk-averaged velocity, and ν is the kinematic molecular viscosity. Thus, the computational requirements for an LES of the viscous sublayer increase at the same rate as those for a DNS, although the local resolution requirements are much lower. In complex high-Reynolds number flows, it will, therefore, be necessary to introduce models for the near-wall viscous sublayer region.

The aim of the present work was to provide a simulation of a test case where wall effects do not dominate and so to contribute towards the development of LES techniques for application in practical engineering problems. A plane jet of air issuing normally into a duct flow has been calculated using LES. A streak line of the flow considered is shown in Figure 1.

As the jet bends, the cross flow is accelerated, because the effective cross-sectional area reduces, resulting in a flow pattern farther downstream which resembles a diffuser, as the main flow is decelerated and re-attaches to the wall. The flow is characterised by the strong shear layers associated with large streamline curvature as well as a large recirculation zone generated by the jet-entraining fluid. This configuration has been previously investigated experimentally by Chen and Hwang (1991) and resembles some of the features of more complex flow fields arising in air conditioning problems or dilution zones of gas turbine combustors. Similar configurations have been studied experimentally by Haniu and Ramaprian (1989) and Patton et al. (1974).

The models used in this work are reviewed in the next section, followed by a description of the calculation methods

---

Address reprint requests to Prof. W. P. Jones, Department of Chemical Engineering and Chemical Technology, Imperial College of Science, Technology and Medicine, London SW7 2BY, UK.

Received 6 November, 1995; accepted 10 February 1996

Int. J. Heat and Fluid Flow 17: 296–306, 1996

655 Avenue of the Americas, New York, NY 10010

0142-727X/96/$15.00
PII S0142-727X(96)00045-7

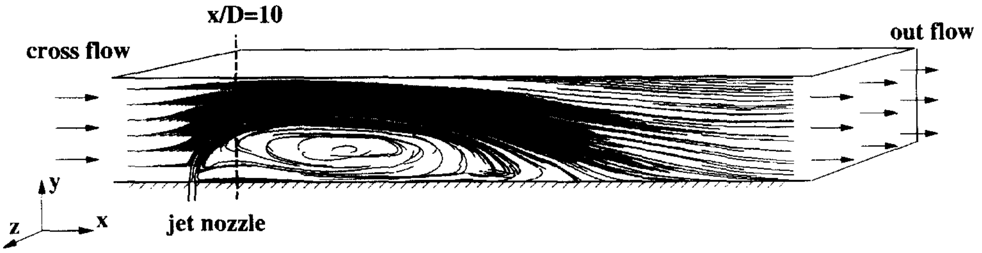

Figure 1 Streak line plot of the single plane jet in a cross-flow

employed, and the flow geometry as well as the boundary conditions used.

Basic equations and modelling

As is well known, the equations for the large-scale motion can be obtained by applying a spatial filter to the Navier–Stokes equations (indicated by an overbar). With a constant filter width, the equations for a constant density fluid are:

$$\frac{\partial \overline{u}_j}{\partial x_j} = 0 \tag{1}$$

$$\frac{\partial \overline{u}_i}{\partial t} + \frac{\partial \overline{u}_i \overline{u}_j + \tau_{ij}}{\partial x_j} = -\frac{1}{\varrho}\frac{\partial \overline{p}}{\partial x_i} + \nu \frac{\partial^2 \overline{u}_i}{\partial x_j^2} \tag{2}$$

Here the residual stresses are given by

$$\tau_{ij} = \overline{u_i u_j} - \overline{u}_i \overline{u}_j \tag{3}$$

and u_i is the velocity, p is the pressure, ν is the kinematic molecular viscosity, and ϱ is the density. The temporal and spatial coordinates correspond to t and x_j, respectively.

A numerical simulation of the flow considered requires a strongly nonuniform mesh in order to resolve the thin jet, while at the same time, covering the larger flow domain. This situation is typical of a number of engineering applications where the geometric scales of the problem vary considerably, and computational resources do not allow uniform mesh spacings that would resolve the smallest geometric scales throughout the flow field. For these flows, the definition of a large-scale flow quantity has to be modified in such a way that the spatial filtering varies with spatial position. Considering the one-dimensional (1-D) case for brevity, a spatial average can be defined with the convolution

$$\bar{f}(x) = \int_{\alpha}^{\beta} G[x - x', \Delta(x)] f(x')\, \mathrm{d}x' \tag{4}$$

where G is the filtering operator, depending on the relative spatial position $(x - x')$ and filter width 2Δ, which as indicated above is a function of position. The filtering is symmetric about x and is mean preserving so that

$$\int_{\alpha}^{\beta} G[x - x', \Delta(x)]\, \mathrm{d}x' = 1,$$

while the integration boundaries α and β are defined suitably (Aldama 1990).

Notation

C_ν, C_ϵ	constants in the one-equation model
C_S	Smagorinsky constant
D	nozzle width
$\bar{f}$	spatially filtered variable
$\langle f \rangle$	ensemble-averaged variable
$G[x - x', \Delta(x)]$	spatial filtering operator
H	duct height
$k = \tau_{ii}/2$	residual stresses kinetic energy
L	length of the solution domain
Pe	Peclet number
p	pressure
$\mathbf{p}$	solution vector for the discrete pressure field
$\boldsymbol{\Delta}\mathbf{p}$	solution vector for the pressure increment
Re	Reynolds number
s_{ij}	strain rate
S	source terms
t	time
$t_\Delta = u_b/L$	residence time
T, D	coefficient matrices
u_j	Cartesian velocity components
u_b	bulk velocity
u_t	tangential velocity component
u'	fluctuating velocity component and rms of the velocity
$u_\Theta = \dfrac{\langle u \rangle - u_b}{\langle u \rangle_{\max} - u_b}$	nondimensional excess velocity
$\mathbf{u}$	solution vector for the discrete velocity field
x_j	Cartesian coordinates
Greek	
α, β	integration boundaries
δ_{sub}	thickness of the sublayer
δ_{ij}	Kronecker delta
δ_t	time increment
Δ_T	length scale for test filter field
$\Delta(x), \Delta$	residual stresses length scale
Δ_S	length scale of Scotti et al. (1993)
ν	kinematic viscosity
ν_t	eddy-viscosity
ϱ	density
τ_{ij}	residual stress tensor
τ_{ij}^a	anisotropic part of τ_{ij}
τ_w	wall shear stress

It is well known that such filtering does not commute with spatial differentiation. Strictly, the filtered equations above should, therefore, contain additional terms corresponding to commutation errors. This can be seen by applying the filtering (Equation 4) to a spatial gradient resulting in

$$\frac{\overline{\partial f(x)}}{\partial x} = \int_{\alpha}^{\beta} G[x-x', \Delta(x)] \frac{\partial f(x')}{\partial x'} \, \mathrm{d}x' \tag{5}$$

so that from integration by parts

$$\frac{\overline{\partial f(x)}}{\partial x} = \underbrace{G[x-x', \Delta(x)] f(x')|_{\alpha}^{\beta}}_{(A)} \underbrace{- \int_{\alpha}^{\beta} f(x') \frac{\partial G[x-x', \Delta(x)]}{\partial x'} \, \mathrm{d}x'}_{(B)} \tag{6}$$

The first term (A) vanishes, because $G[x-x', \Delta(x)]f = 0$ on the integration boundaries α, β. Applying the chain rule to the remaining term (B) then results in

$$\begin{aligned} \frac{\overline{\partial f(x)}}{\partial x} &= \frac{\partial}{\partial x} \int_{\alpha}^{\beta} f(x') G[x-x', \Delta(x)] \, \mathrm{d}x' \\ &\quad - \int_{\alpha}^{\beta} f(x') \frac{\partial G[x-x', \Delta(x)]}{\partial \Delta} \frac{\mathrm{d}\Delta(x)}{\mathrm{d}x} \, \mathrm{d}x' \\ &= \frac{\partial \bar{f}(x)}{\partial x} - \frac{\partial \bar{f}(x)}{\partial \Delta} \frac{\mathrm{d}\Delta}{\mathrm{d}x}(x) \end{aligned} \tag{7}$$

since

$$\frac{\partial G[x-x', \Delta(x)]}{\partial x'} = \frac{\partial G[x-x', \Delta(x)]}{\partial \Delta} \frac{\mathrm{d}\Delta(x)}{\mathrm{d}x} - \frac{\partial G[x-x', \Delta(x)]}{\partial x} \tag{8}$$

This expression can easily be expanded to three spatial dimensions. Thus, the averaging process with a filter width varying continuously in space introduces terms of the form

$$\frac{\partial \bar{f}}{\partial \Delta} \frac{\mathrm{d}\Delta}{\mathrm{d}x}$$

to the equations where $(\partial \bar{f} / \partial \Delta)$ is of the same order as the spatial derivatives in the smallest resolved wave numbers.

Some authors (Ghosal et al. 1995) redefine the filtering operation so that the physical space corresponding to the nonuniform filter width is mapped onto a computational space, where the filter width is no longer a function of position so that the spatial filtering can be applied in the usual manner. This results in filter functions of the form $G[x-x', \Delta(x, x')]$ in physical space, which are biased towards finer mesh resolution. The leading term of an expansion of the commutation error associated with this kind of filter can be shown to scale on Δ^2. Also, as pointed out by van der Ven (1995), a family of filters can be constructed for which the commutation error scales on an arbitrary power of Δ. However, the physical interpretation of the resulting filtered fields is ambiguous. It is not clear how these filter definitions affect the size of the terms in the equations in relation to the commutation error, in particular the size of the residual stresses.

In the present work, the commutation errors are neglected. On the rectangular mesh used for some of the simulations, the spacing varies smoothly. Mesh expansion ratios lie between 0.9 and 1.1, so that $(\mathrm{d}\Delta/\mathrm{d}x)$ is small, and commutation errors are about an order of magnitude smaller than the associated spatial derivative terms. On the adaptive mesh, the expansion ratios are locally much larger so that the commutation error can become significant in the smallest wave numbers. It is argued that, in this case, numerical errors become large in the smallest resolved wave numbers also so that an explicit treatment of commutation terms is not justified.

To close the filtered transport equation, the anisotropic part of the residual stresses

$$\tau_{ij}^{a} = \tau_{ij} - \tfrac{2}{3}\delta_{ij}k \tag{9}$$

is approximated alternatively by a standard Smagorinsky–Lilly model, a dynamic model and a one-equation model. These eddy-viscosity models can be cast into the following form

$$\tau_{ij}^{a} = -2\nu_t \bar{s}_{ij} \tag{10}$$

where ν_t is the eddy-viscosity, and $s_{ij} = (1/2)[(\partial u_i/\partial x_j) + (\partial u_j/\partial x_i)]$ is the strain rate. The isotropic part of the residual stresses $[(2/3)\delta_{ij}k]$ was included in the pressure term in the usual manner.

The standard Smagorinsky–Lilly model (Smagorinsky 1963) was written as

$$\tau_{ij}^{a} = -2(C_S\Delta)^2\sqrt{2}|\bar{s}_{ij}|\bar{s}_{ij} \tag{11}$$

where a characteristic length scale for the smallest resolved motion was obtained from

$$\Delta = (\Delta x \, \Delta y \, \Delta z)^{1/3} \tag{12}$$

a measure for the local mesh refinement. Alternatively, the length scale Δ_S suggested by Scotti et al. (1993) was used to account for grid anisotropy. With equilibrium assumptions (Schmidt and Schumann 1989) a value of $C_S = 0.165$ was calculated assuming that 2Δ is the smallest resolvable wave length. This value was increased to $C_S = 0.3$ in two of the simulations presented below.

For the dynamic model, an approach suggested by Piomelli and Liu (1995) was adopted where the Smagorinsky parameter C_S in Equation 11 was evaluated dynamically from

$$(C_S\Delta_T)^2 = \frac{\left\{\left[(C_S^{*}a\Delta)^2|\bar{s}_{ij}|\bar{s}_{ij}\right]^{\sim} - \mathscr{L}_{ij}^{a}2^{-3/2}\right\}\tilde{\bar{s}}_{ij}}{|\tilde{\bar{s}}_{ij}|^3} \tag{13}$$

Here, Δ_T is the filter width for the test field (test filtering is indicated by a tilde or $[\ ]^{\sim}$), and $\mathscr{L}_{ij}^{a}$ is the anisotropic resolved part of the test field residual stress described by Germano's identity (Germano et al. 1991). This expression is obtained in the usual manner; i.e., by introducing a test filter field, invoking a gradient assumption for the residual stresses and applying a least-squares minimisation to Germano's identity. The above equation was solved by iterating twice, taking the most recent value of C_S for C_S^{*} in the test-filtering operator on the right-hand side of the equation. The test field was obtained by averaging over adjacent mesh cells, corresponding to the use of a box filter with a width of $\Delta_T \approx 3\Delta$. Negative values of C_S where clipped to zero, to avoid the appearance of negative viscosities which correspond to "explosive"-type physical phenomena.

For the one-equation model (Schmidt and Schumann 1989) the closed form of the transport equation for the residual stresses energy k was solved to obtain a velocity scale for the eddy-viscosity and the anisotropic part of the residual stresses was then approximated with

$$\tau^a_{ij} = -2(C_\mu k^{1/2}\Delta)\bar{s}_{ij} \tag{14}$$

The transport equation for k is

$$\frac{\partial k}{\partial t} + \frac{\partial k\bar{u}_j}{\partial x_j} = -\tau_{ij}\bar{s}_{ij} + \frac{\partial}{\partial x_j}\left(\left(\frac{\nu_t}{\sigma_t} + \nu\right)\frac{\partial k}{\partial x_j}\right) - C_\epsilon \frac{k^{3/2}}{\Delta} \tag{15}$$

where $\sigma_t = 0.7$ is a turbulent Prandtl number. The constants C_ϵ and C_μ appearing in the above equations were evaluated from equilibrium assumptions as suggested by Schmidt and Schumann and were assigned the values

$$C_\mu = 0.0856 \qquad C_\epsilon = 0.845 \tag{16}$$

Calculation methods

A finite volume method was used to obtain a solution of the spatially averaged Navier–Stokes equations written in terms of general curvilinear coordinates. A nonstaggered mesh arrangement was adopted in conjunction with a pressure-smoothing technique of the type proposed by Rhie and Chow (1983) to prevent odd–even decoupling of the pressure and velocity fields; velocities and pressure were stored at cell centres.

The discretisation of the convection terms is a potential source of numerical error in LES calculation and a subject of debate. Flux limiting or TVD-type schemes (Jones 1994), which improve numerical accuracy in Reynolds average calculations considerably, fail for LES calculations (Sandham and Yee 1983) unless the resolution is very high (Boris et al. 1992). As with other asymmetric approximations to the convection terms, they introduce damping to the discretised equations which scales with the cell Peclet number $\mathrm{Pe} = u_i \Delta x/\nu$ (Shyy 1985). This can remove a large part of the turbulence and even lead to a predicted but unphysical laminarisation. It is well known that although central differences are free from "numerical" diffusion, the corresponding solutions can exhibit oscillatory behaviour (Leonard and Mokhtari 1990). However, many workers have obtained satisfactory results using second-order central differences for the convection terms. Higher-order symmetric schemes give rise to large errors in the smallest simulated scales if these are not well resolved and thus do not seem to offer a prospect of improved numerical accuracy in the LES computations considered. Therefore, in the present work, all spatial terms were approximated via second-order central differences, except for the convection terms in the k-equation. These were represented by a TVD-type approximation to avoid nonphysical negative values of k.

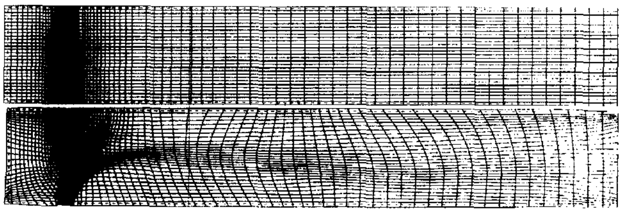

Figure 2 Computational mesh with 87 × 30 × 30: a) rectangular mesh; b) adapted on the arc length of the mean velocity

An implicit difference scheme was utilised with time derivatives being represented by the second-order accurate three-point backward difference approximation:

$$\frac{\partial u}{\partial t} \approx \frac{3}{2}\frac{u^{n+1} - u^n}{\delta t} - \frac{1}{2}\frac{u^n - u^{n-1}}{\delta t} + O(\delta t^2) \tag{17}$$

The difference equations resulting from the discretisation are written using matrix notation, so that, for example, for the u-component

$$\mathbf{u}^{n+1} - \mathbf{u}^n + \tfrac{2}{3}\delta t T \mathbf{u}^{n+1} = -\tfrac{2}{3}\delta t D \mathbf{p}^{n+1} + S \tag{18}$$

Here T, D, and S are finite difference coefficients, where T corresponds to convection and diffusion, D is associated with the pressure gradient, and S represents any remaining terms, including the cross-stresses not contained within T. If T and S are evaluated at time t_{n+1}, this is a second-order accurate approximation in time to the momentum transport equation.

To devise a solution algorithm, the above equation is first expressed in terms of the pressure differences $\mathbf{\Delta p} = \mathbf{p}^{n+1} - \mathbf{p}^n$ so that

$$(I + \tfrac{2}{3}\delta t T)\mathbf{u}^{n+1} + \tfrac{2}{3}\delta t D \mathbf{\Delta p} = \mathbf{u}^n - \tfrac{2}{3}\delta t D \mathbf{p}^n + S \tag{19}$$

To solve this system of equations, an approximate factorisation is then applied:

$$(I + \tfrac{2}{3}\delta t T)\underbrace{(\mathbf{u}^{n+1/2} + \tfrac{2}{3}\delta t D \mathbf{\Delta p})}_{u^*} = \mathbf{u}^n - \tfrac{2}{3}\delta t D \mathbf{p}^n + S \tag{20}$$

and this system of equations is solved in two steps:

$$\mathbf{u}^* = (I + \tfrac{2}{3}\delta t T)^{-1}(\mathbf{u}^n - \tfrac{2}{3}\delta t D \mathbf{p}^n + S) \tag{21a}$$

$$\mathbf{u}^{n+1/2} = \mathbf{u}^* - \tfrac{2}{3}\delta t D \mathbf{\Delta p} \tag{21b}$$

Equation 21a is solved here with the elements of T and S evaluated in terms of the most recent solutions available to yield $\mathbf{u}^*$. A similar approach is adopted for v^*, etc. The resulting velocity field is used in conjunction with Equation 21b and is substituted into the continuity equation resulting in a Poisson equation which is solved to yield the pressure increment $\mathbf{\Delta p}$ from which the solution $\mathbf{u}^{n+1/2}$ corresponding to a mass-conserving velocity field is calculated. The index $n + \frac{1}{2}$ has been introduced here to indicate an interim solution obtained through evaluation of some of the coefficient matrices in terms of the solution at time t_n, which results in a truncation error in $\mathbf{u}^{n+1/2}$ and $\mathbf{p}^{n+1/2}$, which is $O(\delta t^2)$. This corresponds to a first-order error to the difference Equation 19 and, thus, to a first-order approximation to the differential equation.

To maintain second-order accuracy a second-stage factorisation is applied where the coefficients are now evaluated in terms of $\mathbf{u}^{n+1/2}$ etc. and where now $\mathbf{\Delta p} = \mathbf{p}^{n+1} - \mathbf{p}^{n+1/2}$, so that

$$(I + \tfrac{2}{3}\delta t T)\mathbf{u}^{n+1} + \tfrac{2}{3}\delta t D \mathbf{\Delta p} = \mathbf{u}^n - \tfrac{2}{3}\delta t D \mathbf{p}^{n+1/2} + S \tag{22}$$

This equation is then solved as above in Equation 21a and 21b to give the solution at t_{n+1}. The difference between the solution arising from this two-stage procedure and a fully implicit solution of Equation 19 is of the order of the truncation error in the approximation to the differential equations and can, consequently, be ignored.

The resulting algebraic equations were solved iteratively; a preconditioned conjugate gradient method was used for the pressure difference $\mathbf{\Delta p}$, while the velocity field was solved with a simple line Gauss–Seidel method.

Computational parameters and boundary conditions

Simulations were carried out for a single-plane jet of air issuing perpendicularly into a duct with cross-flowing air. This flow geometry, previously investigated by Chen and Hwang (1991), is depicted in Figure 1, while the coordinate system to describe the flow has its origin at centre of the jet nozzle.

The Reynolds number based on the duct height H and the bulk velocity u_b was Re = 19,000, while the ratio of jet velocity u_j and u_b was 7.34. The Reynolds number for the jet based on the nozzle width D and the bulk exit velocity was Re = 5815. Although the jet was slightly heated in the experiments of Chen and Hwang (1991), Grasshoff numbers were small, so that density variations were considered negligible and, thus, not included in the calculations.

The duct in the experiments of Chen and Hwang (1991) extended over two heights H in the spanwise direction, but they found the flow to be 2-D over most of the cross section. To reduce computational cost, the problem was, therefore, treated as an infinite channel, thus neglecting the secondary motion induced by the duct side walls. Calculations were performed on a domain covering one duct height in the spanwise direction, and periodic conditions were applied in this direction.

In the streamwise x-direction, the domain covered one duct height upstream of the jet exit and extended 5.15 duct heights downstream of the jet exit, corresponding to the experimental configuration. Relatively coarse meshes were used with $87 \times 30 \times 30$ grid nodes in the streamwise, the wall-normal, and the spanwise directions, respectively. Initially, a rectangular mesh was used which was refined in the vicinity of the jet and smoothly expanded towards the inflow and outflow boundaries. Results from calculations with this mesh were then used to generate a mesh adapted on the solution arc length of the magnitude of the velocity vector (Menzies 1996).

Wall boundaries were approximated using Grötzbach's (1983) approach, because computational resources did not allow for a resolution of the viscous sublayer. The wall shear stress τ_w was, thus, assumed to be linearly related to the instantaneous spatially averaged tangential velocity $\bar{u}_t$ at the first grid node adjacent to the wall, so that

$$\tau_w = \frac{\bar{u}_t}{\langle \bar{u}_t \rangle} \langle \tau_w \rangle \tag{23}$$

Here $\langle \bar{u}_t \rangle$ is the time mean average of the tangential velocity component, and the mean wall shear stress $\langle \tau_w \rangle$ was obtained assuming a semilogarithmic profile for $\langle \bar{u}_t \rangle$. This approach has been found to give reasonable results in plane channel and pipe flows, and in addition, it was felt that the flow around the jet would be largely uninfluenced by the details of the wall flow.

At the inflow an instantaneous velocity $\bar{u}_i = \langle u_i \rangle + u'_i$ was specified in a manner similar to that used by Lee et al. (1992). The fluctuating component u'_i as obtained by calculating the inverse fast Fourier transform (FFT) of a randomly generated homogeneous velocity field in wave space, and the result was

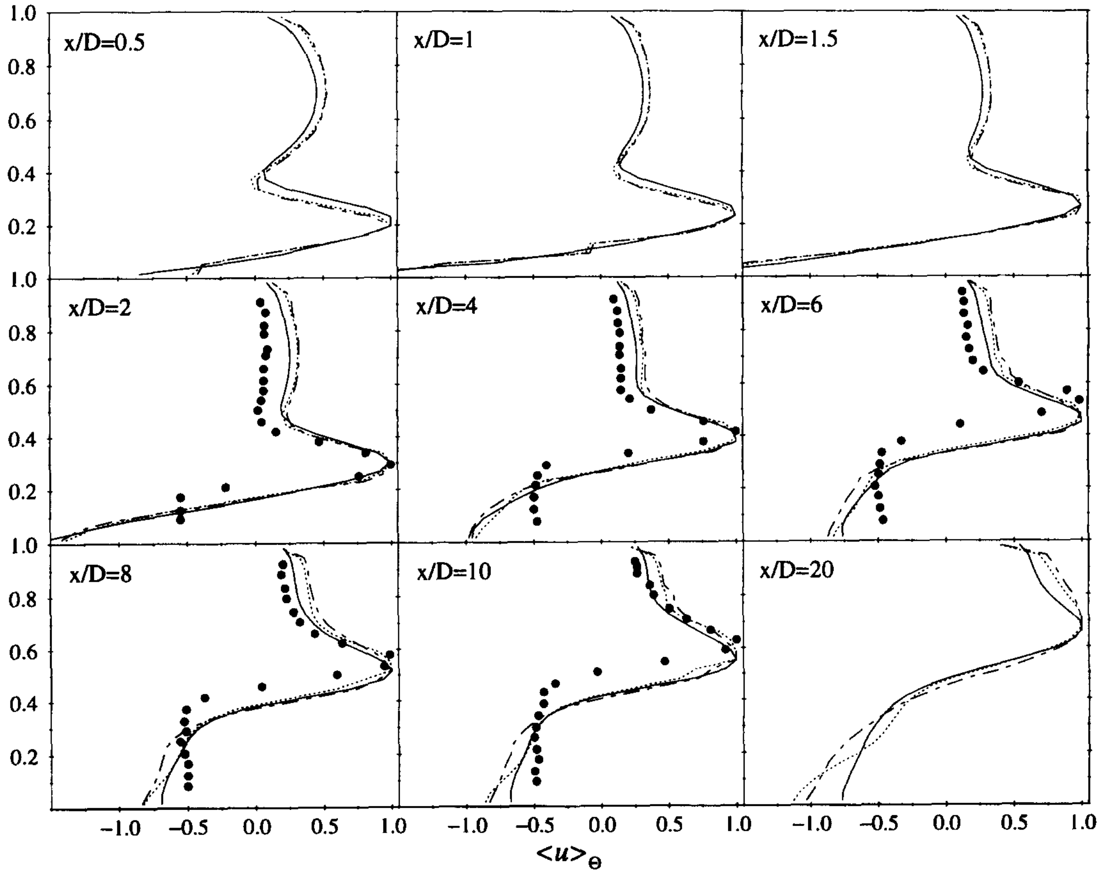

Figure 3 Normalised mean axial velocity at positions x/D downstream of the jet exit; y/H nondimensional distance from the wall; ● measurements by Chen and Hwang (1991); —— rectangular mesh, Smagorinsky–Lilly model, C_S=0.3, Δ; ----- adapted mesh, Smagorinsky–Lilly model, C_S=0.3, Δ; –·– adapted mesh, Smagorinsky–Lilly model, C_S=0.165, Δ_S

scaled to be consistent with the rms values observed in plane channel flow. As an alternative, a fully developed channel flow was monitored and used to provide in-flow conditions for the cross-flow. The results obtained using the two methods were practically identical with regard to the first and second moments. As anticipated, this indicates that the turbulence production in the shear layers surrounding the jet remains largely uninfluenced by the turbulence of the incoming cross-flow. Changes in the turbulence properties at the jet inlet also had negligible effect. A nonreflecting convective condition (Jin and Braza 1993) was used at the outflow.

Compared to simpler problems, the cost for the LES computation in terms of CPU time was considerably increased, particularly because a fine computational mesh was required to resolve the flow around the jet exit. To maintain temporal accuracy, the maximum Courant number was maintained at about 0.3, and this resulted in a small time-step.

Results

In this section, the results from the LES for different meshes and runs with the different models described above are compared to measurements. The total integration time corresponded to at least four residence times $t_\Delta = (u_b/L)$, where L is the length of the solution domain, and u_b is the bulk velocity of the cross-flow. After $t_\Delta = 2.5$, the solution was assumed to be statistically stationary, because profiles for first and second moments did not change significantly for about $t_\Delta = 1$. Calculations were then continued for at least another 1.5 residence times to obtain statistical quantities. The statistical sample size was increased by averaging in the homogeneous (spanwise) direction.

Chen and Hwang (1991) measured the axial velocity component and present their mean data in the form of a nondimensional excess velocity

$$u_\Theta = \frac{\langle u \rangle - u_b}{\langle u \rangle_{\max} - u_b} \tag{24}$$

where u_b is, again, the bulk velocity of the cross-flow and $\langle u \rangle_{\max}$ is the local maximum of the mean axial velocity component in a cross section at a downstream location x/D. The turbulent axial fluctuations they measured were presented as intensities $u'/\langle u \rangle_{\max}$, where u' is the rms value of the velocity. This notation was adopted in the present work to compare measured and simulated data. It is worth noting here that the measurements only cover a short distance $x/D = 10$ downstream of the jet nozzle (cf. Figure 1), and thus, it was impossible to draw any conclusions concerning the predicted flow in regions farther away from the jet exit.

Adapted mesh

Initial simulations were carried out on a rectangular mesh, and the solution was used to generate an adapted mesh. Both meshes are shown in Figure 2. It can be observed that the spacings in both meshes must vary strongly, because the slot through which

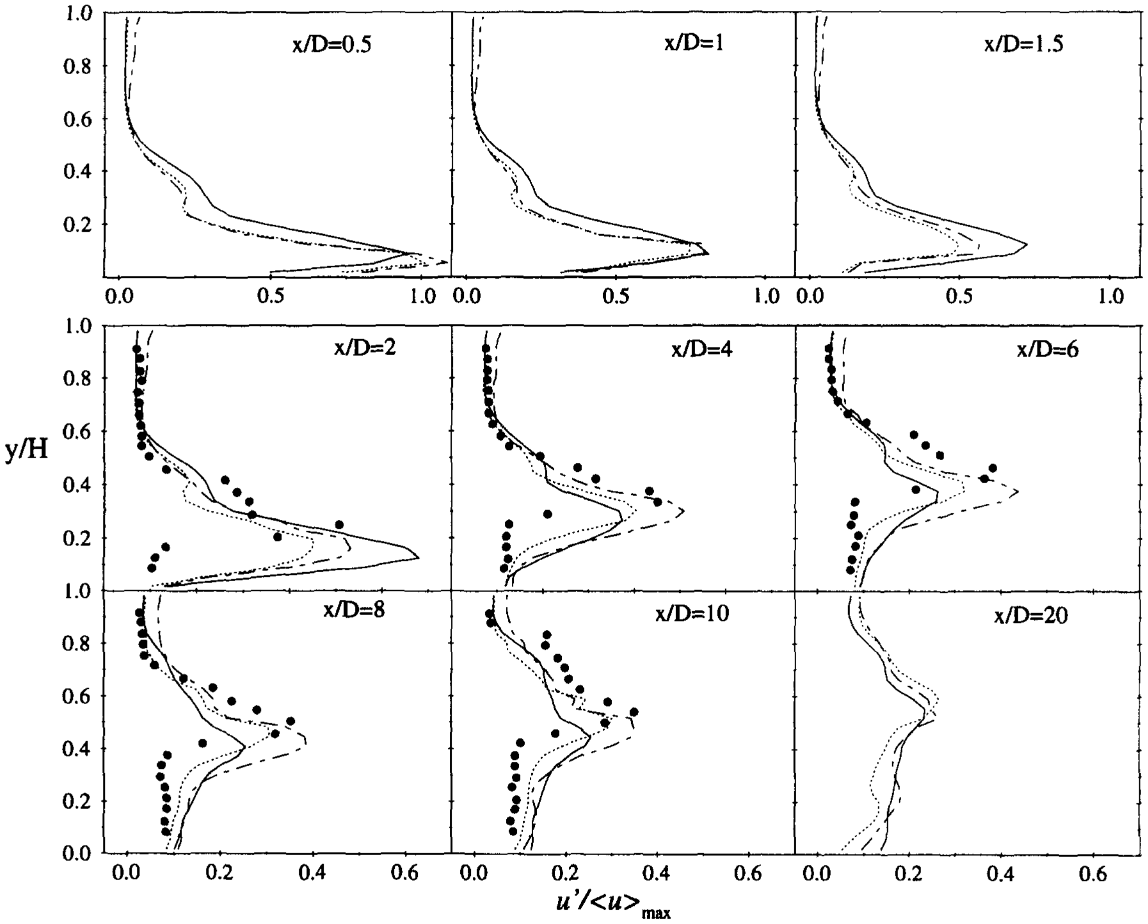

Figure 4 Normalised axial turbulent intensity at various positions x/D downstream of the jet exit; y/H nondimensional distance from the wall; for legend see Figure 3

the jet exits is only 5-mm wide, while the computational domain is 715-mm long. The geometric scales of the problem, thus, vary by two orders of magnitude. It can also be seen that the number of grid nodes in the jet shear layer increased dramatically with the mesh adaptation so that the number in the jet exit rose from 8 nodes on the rectangular mesh to 33 for the adapted mesh.

Results from calculations with the Smagorinsky–Lilly model on both a rectangular and adapted mesh are shown in Figures 3 and 4. The simulation on the rectangular mesh and the first simulation on the adapted grid were carried out with a value of $C_S = 0.3$ and Δ (Equation 12) used as a length scale for the residual stresses. The results for the second simulation on the adapted mesh shown in the figure were obtained with a Smagorinsky constant of $C_S = 0.165$ and the length scale Δ_S modified according to Scotti et al. (1993) to account for mesh anisotropy. Profiles for $\langle u \rangle_\Theta$ and $u'/\langle u \rangle_{\max}$ are plotted against the nondimensional wall normal direction y/H at several distances x/D downstream of the jet exit.

The mean velocity profiles indicate that the part of the flow corresponding to the accelerated cross-flow is reproduced reasonably well in all predictions. The results for the simulation on the rectangular mesh show slightly better agreement with the measured data, but the difference between measured and predicted data cannot be identified with certainty because of the normalisation used for the measurements. The maximum velocity of the jet is probably underpredicted in all calculations and, thus, would explain the observed discrepancies between measured and predicted profiles.

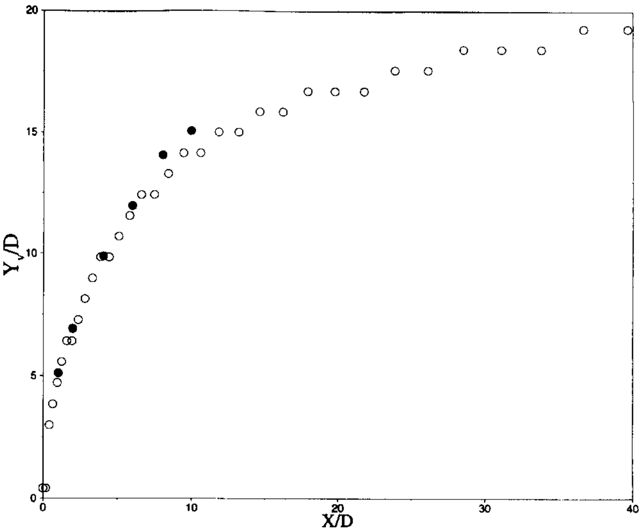

Figure 5 Jet trajectory; ● measurements; ○ predictions

The inner part of the flow corresponding to the recirculation region shows larger disagreement. Whilst the measurements indicate an almost constant reverse flow toward the shear layer, all the predictions display profiles consistent with a solid body rotation typical of the recirculation zones found in flows, such as that over a backward facing step. Again, differences between various predictions are visible, but generally they are smaller than the deviations from the measured data. With all residual stress models, the predicted jet trajectory coincides with the measurements close to the jet exit, but farther downstream, the predicted jet path is bent more by the cross-flow than is observed in the measurements. This can be seen in Figure 5 where the location $y_{\max}$ for the grid node with the maximum velocity $|u|$ is plotted as a function of downstream distance x and compared with the measurements. This behavior is accompanied by a general overprediction of the spreading rate. A more slender jet is predicted with the adapted mesh at stations close to the jet exit, $x/D = 0.5$, $x/D = 1$, and $x/D = 1.5$, which must be attributed to the much finer resolution around the jet exit achieved

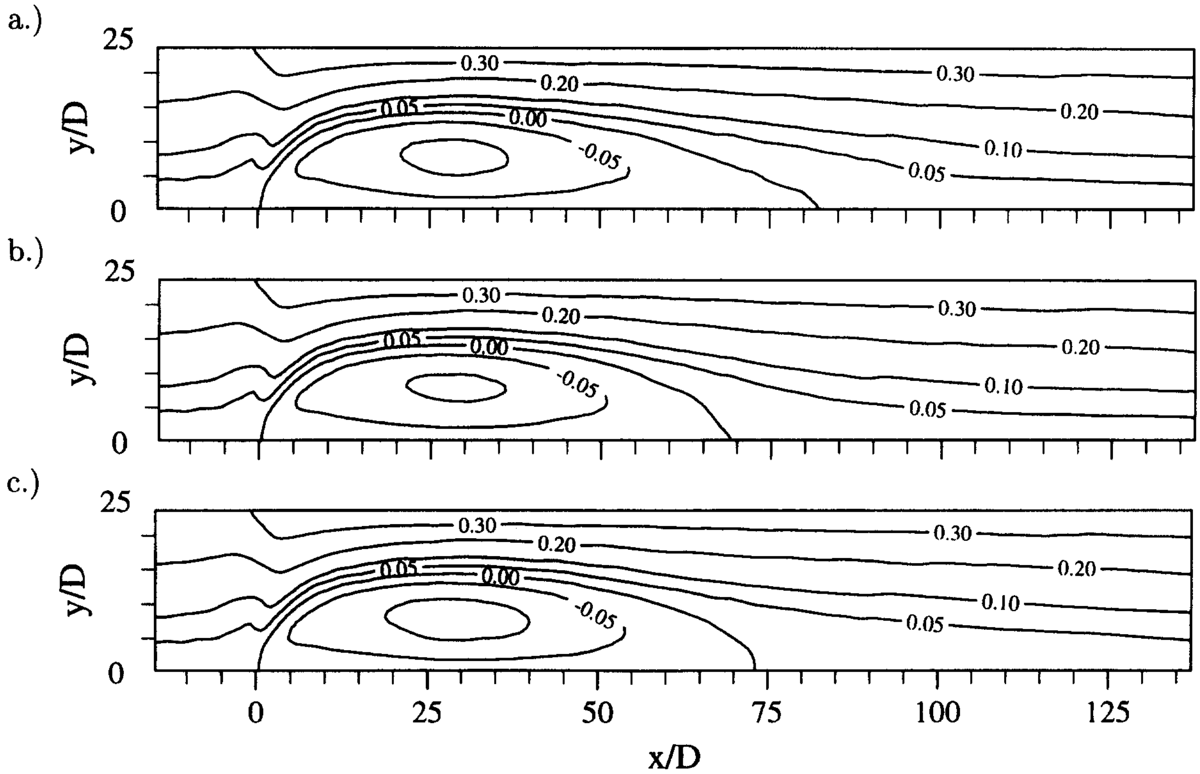

Figure 6 Streamlines for predictions on adapted grid: a) Smagorinsky–Lilly model; b) one-equation model; c) dynamic model

with this mesh. Farther downstream, the simulations on the adapted grid show a larger spreading rate, as compared to the results obtained with the rectangular mesh. In this region, the adapted mesh is coarser, as can be seen in Figure 2, and, consequently, the flow resolution is poorer. The axial velocity fluctuations confirm this interpretation. In Figure 4, the normalised rms values are plotted at various stations x/D downstream of the jet exit. At distances up to $x/D = 2$, turbulent fluctuations are predicted to be stronger on the rectangular mesh than those calculated with the adapted mesh, in the axial as well as the spanwise and the wall-normal components (not shown here). Farther downstream, maximum values of turbulent fluctuations fall below those obtained with the adapted mesh and are largely consistent with the observed spreading of the jet. It is also apparent that the location of the simulated shear layers do not coincide with the measurements in all simulations. The maxima in the plotted profiles indicate that the shear layer on the concave side of the jet is predicted to be closer to the wall than is observed in the measurements. In addition, the fluctuations on the concave side of the jet are overpredicted in all shown simulations. Both of these observations are associated with the large mean gradient predicted in this area, resulting in large turbulence production and, thus, higher fluctuations than observed in the measurements. However, qualitatively, the predicted shapes of the profiles are consistent with the stabilising and destabilising effects of streamline curvature observed experimentally. On the convex side, the velocity fluctuations spread into the cross stream, while on the concave side, a much more rapid fall in turbulent intensities is observed. A similar behaviour can be seen from the mean profiles.

To compare the different residual scale models, further calculated were undertaken on the adapted mesh, because this, in general, gave slightly more realistic values for the turbulent fluctuations.

Residual scale closures

The introduction of a length scale Δ_S modified to account for mesh anisotropy (Scotti et al. 1993) had virtually no effect on the predicted statistics. Results, not shown here, using a Smagorinsky constant $C_S = 0.165$ with the length scale Δ, defined in Equation 12, were virtually indistinguishable from those obtained using an adjusted length scale Δ_S, shown in Figures 3 and 4.

In Figures 6–8 results for simulations with $C_S = 0.165$ and Δ_S are compared to results obtained using the one-equation model and the dynamic model described in the Basic equation and modelling section. For the dynamic model and the one-equation model, a simple length scale Δ was used. Figure 6 shows mean streamlines for the different simulations, and Figures 7 and 8 show profiles for the mean and rms values of the axial velocity component. It is clear from these figures that differences between the various predictions are largest in the far field of the flow. In the simulations with the Smagorinsky–Lilly model, the jet attaches to the wall at $x/D = 82$, while the one-equation and the dynamic model result in a somewhat shorter recirculation zone.

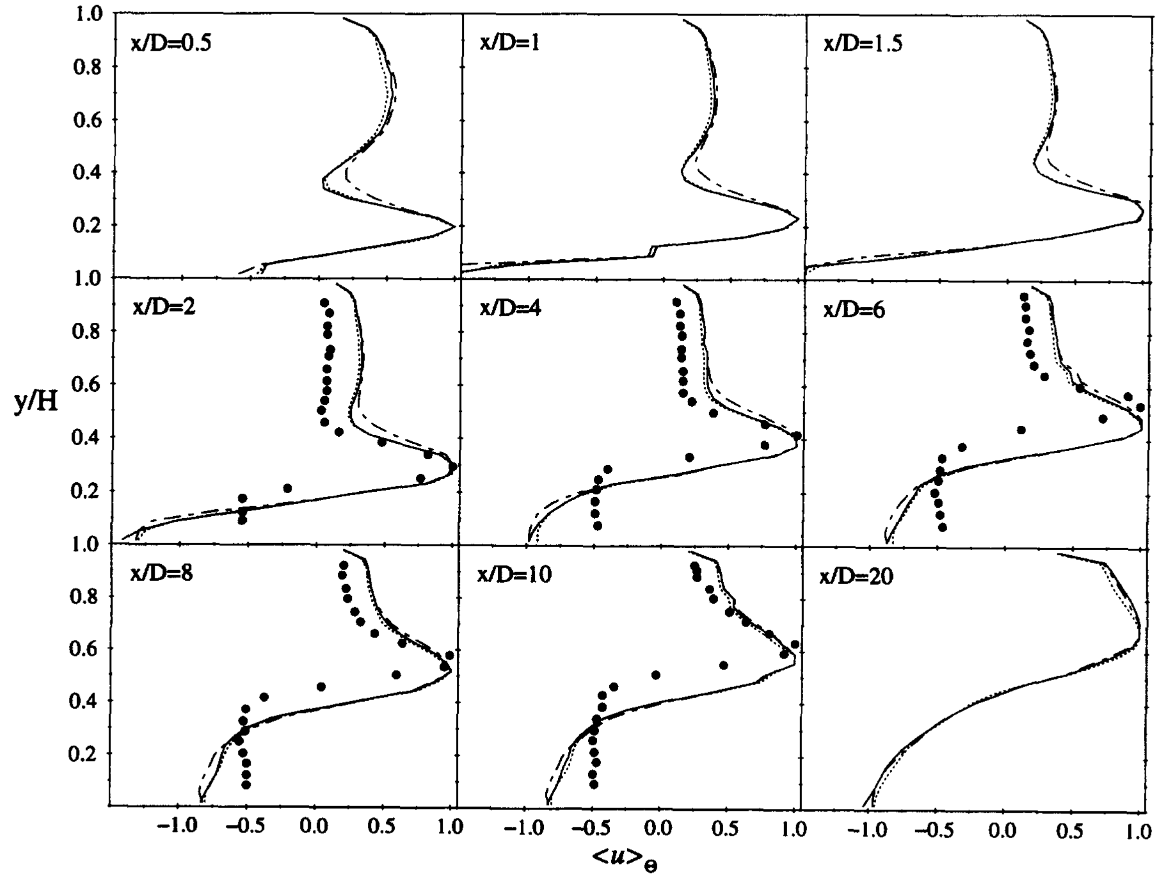

Figure 7 Normalised mean axial velocity at positions x/D downstream of the jet exit: y/H nondimensional distance from the wall; ● measurements by (Chen and Hwang 1991); —— Smagorinsky–Lilly model; ----- one-equation model; –·– dynamic model

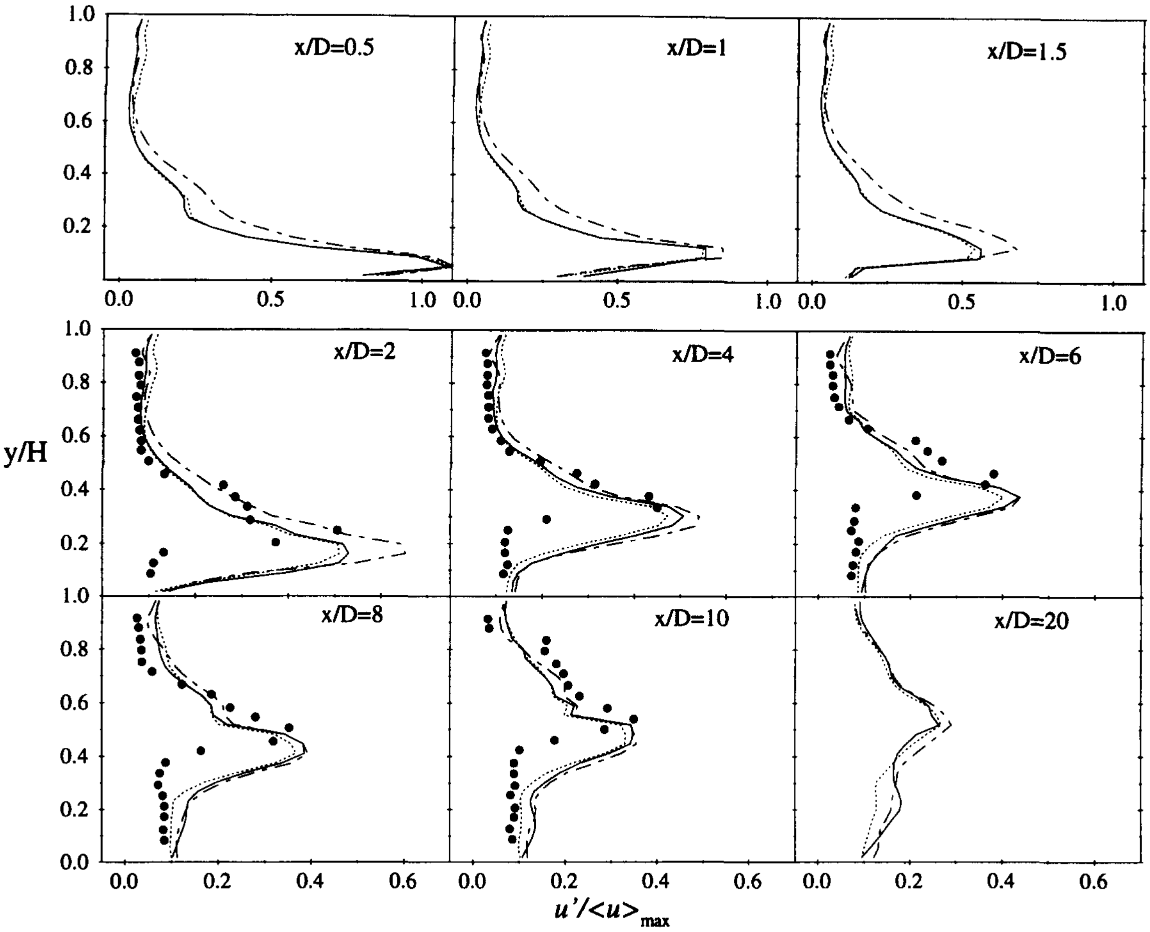

Figure 8 Normalised axial turbulent intensity at various positions x/D downstream of the jet exit; y/H nondimensional distance from the wall; for legend see Figure 7

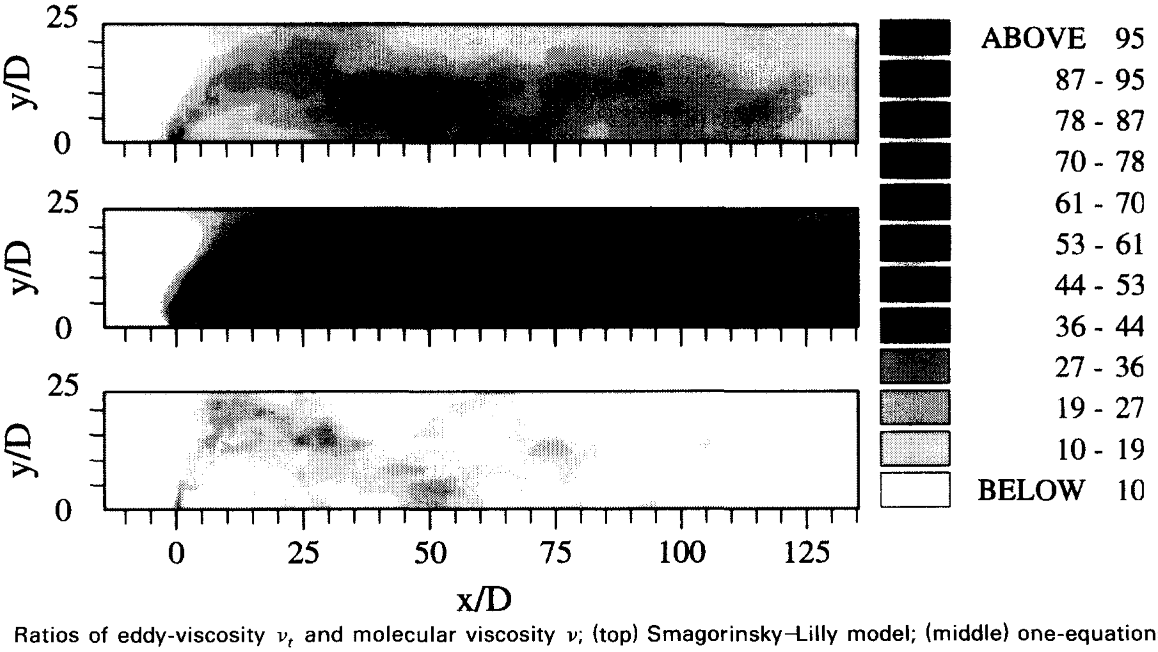

Figure 9 Ratios of eddy-viscosity ν_t and molecular viscosity ν; (top) Smagorinsky–Lilly model; (middle) one-equations model; (bottom) dynamic model

Close to the jet exit, the one-equation model and the Smagorinsky–Lilly model give virtually identical mean axial velocity profiles, as can be observed in Figure 7. The results with the dynamic model differ only slightly, although this model predicts a more rapid mixing of the jet and the cross-flow, as can be seen from profiles for $x/D = 0.5$ to $x/D = 1.5$. This is accompanied by larger fluctuations u' on the convex side of the mixing layer and slightly larger maxima for the axial fluctuations at locations $x/D = 1$ to $x/D = 4$ with the dynamic model compared to the other models. The figures also show that the one-equation model gives slightly more realistic results for the axial intensities in the recirculation zone.

Although the predicted statistics are similar, the various models generate considerably different eddy-viscosities. This can be seen in Figure 9, where contours are plotted for the ratio (ν_t/ν) of the residual scale eddy-viscosity and the molecular viscosity. The eddy-viscosities shown were calculated for one realisation in time for each simulation and averaged in the homogeneous direction. As can be observed, the one-equation model introduces the largest residual stresses relative to the viscous terms, while the dynamic model generally predicts the lowest ratio, particularly away from the jet exit. However, the eddy-viscosities obtained with the dynamic model vary rapidly with position. Values up to $(\nu_t/\nu) = 400$ are predicted locally, and these values are considerably larger than those resulting from the other models. The levels of damping introduced by the residual scale models are partly reflected in the predicted levels of turbulent fluctuations. The one-equation model results in lower maximum values for the turbulent stresses and produces lower oscillations in the recirculation zone than do the other two models, while the dynamic model generated increased fluctuations, as can be seen from the profile of u' in Figure 8.

The ratios (ν_t/ν) plotted in Figure 9 indicate that the dissipation introduced with the residual scale modelling is at least an order of magnitude larger than is the case in simple configurations, such as channel flows, where the average eddy-viscosity is generally of the same order as the molecular viscosity. It is essentially for this reason that solutions obtained without any residual scale model exhibited large nonphysical oscillations in the present case. This is quite unlike the behaviour in, for example, plane channel flows where the effects of omitting the residual scale model are generally small. In the present case, the occurrence of nonphysical oscillations was particularly pronounced for simulations on the rectangular mesh so that a large value of $C_S = 0.3$ had to be used to account for unresolved turbulence in the shear layer around the jet exit.

It is interesting to note that the overall level of kinetic energy dissipated by means of the residual scale model has a larger effect on the statistics than the details of the turbulence model itself. In a comparison of the results form the adapted mesh in Figures 3, 4, 7, and 8, it can be seen that a change in the Smagorinsky constant from its equilibrium value of $C_S = 0.165$ to $C_S = 0.3$ has a larger effect on the turbulence fluctuations and the mean velocities than replacing the Smagorinsky–Lilly with the one-equation model; this is with model constant values for both models based upon equilibrium assumptions (Schmidt and Schumann 1989).

Conclusions

Large-eddy simulations of a plane jet in a cross-flow were carried out with a synthetic inflow condition and approximate wall boundary conditions. Reasonable agreement was obtained, despite a relatively coarse mesh and simple model assumptions for the residual stresses. Integration times were large because of the fine mesh required around the jet exit and the associated small time-steps.

It was found that adapting the mesh to the solution arc length of the mean velocity in order to increase the numerical resolution in the vicinity of the jet exit had only a small effect on the results. A probable cause of this is that the mesh adaptation resulted in a local refinement in the mean shear layers developing around the jet at the expense of reduced resolution in the other regions. For example, numerical resolution was reduced in the recirculation region and the cross-flow region away from the jet on the adapted mesh when compared to the rectangular one. Also, in the present case, the mesh was only refined in two dimensions, and the adaptation resulted in a strongly anisotropic grid. As a consequence, little benefit appeared to result from the mesh adaptation. The mean velocity field is probably not the optimum parameter for mesh refinement in LES computations.

The various residual stress models were found to have only a small effect on the predicted results, despite the fact that they gave rise to very different values for the residual scale eddy-viscosity. However, all residual scale models dissipate a significant level of resolved turbulence energy, and for the mesh sizes used in the present work, residual scale modelling is essential to prevent an accumulation of turbulent kinetic energy in the large scales and corresponding nonphysical oscillations. The Smagorinsky–Lilly model and the residual turbulent energy transport equation model produced very similar results, although the transport equation model resulted in a slightly improved prediction of turbulence quantities. The simulations generated with the dynamic model did display differences as compared with those obtained with the other models, but no improvement in the level of agreement with the measured data was achieved. The use of a length scale adjusted to account for mesh anisotropy also had virtually no effect on the results. Overall, these results lend support to the view that LES is relatively insensitive to the residual scale closure in regions remote from solid surfaces.

Acknowledgments

We gratefully acknowledge the support provided by British Gas plc and the EPSRC, under grant number GR/K43903.

References

Akselvoll, K. and Moin, P. 1993. Large-eddy simulation of a backward facing step flow. In *Engineering Turbulence Modelling and Experiments 2*, W. Rodi and F. Martelli (eds.), Elsevier, Florence, Italy, 303–314

Aldama, A. 1990. *Filtering Techniques for Turbulent Flow Simulation*. Lecture Notes in Engineering, Vol. 56, C. A. Brabbia and S. A. Orszag (eds.), Springer-Verlag, Berlin, Heidelberg, New York

Boris, J., Grinstein, F., Oran, E., and Kolbe, R. 1992. New insights into large-eddy simulation. *Fluid Dyn. Res.*, **10**, 199–228

Breuer, M. and Rodi, W. 1994. Large-eddy simulation of turbulent flow through a straight square duct and a 180° bend. In *Direct and Large-Eddy Simulation I*, P. Voke, L. Kleiser, and J.-P. Chollet (eds.), Kluwer Academic, Norwell, MA, 273–286

Chen, K. and Hwang, J. 1991. Experimental study on the mixing of one- and dual-line heated jets with a cold cross-flow in a confined channel. *AIAA J.*, **29**, 353–360

Germano, M., Piomelli, U., Moin, P., and Cabot, W. 1991. A dynamic subgrid-scale eddy-viscosity model. *Phys. Fluids A*, **3**, 1760–1765

Ghosal, S. Lund, T., Moin, P. and Akselvoll, K. 1995. A dynamic localization model for large-eddy simulation of turbulent flows. *J. Fluid Mech.*, **286**, 229–255

Grötzbach, G. 1983. Direct numerical and large-eddy simulations of turbulent channel flows. In *Encyclopedia of Fluid Mechanics*, Vol. 6, N. Cheremisinoff (ed.), Gulf Publishing, West Orange, NJ

Haniu, H. and Ramaprian, B. 1989. Studies on two-dimensional curved nonbuoyant jets in cross-flow. *J. Fluids Eng.*, **111**, 78–86

Härtel, C. and Kleiser, L. 1994. Subgrid-scale modelling in the near-wall region of turbulent wall-bounded flows. In *Direct and Large-Eddy Simulation I*, (P. Voke, L. Kleiser and J.-P. Chollet (eds.), Kluwer Academic, Norwell, MA, 97–108

Jin, G. and Braza, M. 1993. A nonreflecting outlet boundary condition for incompressible unsteady Navier–Stokes calculations. *J. Comp. Physics*, **107**, 239–253

Jones, W. 1994. Turbulence modelling and numerical solution methods for variable density and combusting flows. In *Turbulent Reactive Flows*, P. A. Libby and F. A. Williams (eds.), Academic, Orlando, FL, 309–374

Lee, S., Lele, S. and Moin, P. 1992. Simulation of spatially evolving turbulence and the applicability of Taylor's hypothesis in compressible flow. *Phys. Fluids A*, **4**, 1521–1530

Leonard, B. and Mokhtari, S. 1990. Beyond first-order upwiding: The ultrasharp alternative for nonoscillatory steady-state simulation of convection. *Int. J. Numer. Methods Eng.*, **30**, 729–766

Manhart, M. and Wengle, H. 1993. A spatiotemporal decomposition of a fully inhomogeneous turbulent flow field. *Theoret. Comp. Fluid Dynamics*, **5**, 223–242

Menzies, K. 1996. Ph.D. thesis, Imperial College of Science, Technology and Medicine, London, UK, in preparation

Patton, A., Test, F. and Hagist, 1974. An experimental investigation of a heated two-dimensional water jet discharge into a moving stream. *J. Heat Transfer*, 273–278

Piomelli, U. 1987. Models for Large-Eddy Simulations of turbulent channel flows including transpiration. Ph.D. thesis, Stanford University, Stanford, CA

Piomelli, U. and Liu, J. 1995. Large-eddy simulation of rotating channel flows using a localized dynamic model. *Phys. Fluids*, **7**, 839–848

Rhie, C. and Chow, W. 1983. Numerical study of the turbulent flow past an airflow with trailing edge separation. *AIAA J.*, **21**, 1525–1532

Rogallo, R. and Moin, P. 1994. Numerical simulation of turbulent flow. *Ann. Rev. Fluid Mech.*, **16**, 99–137

Sandham, N. and Yee, H. 1989. A numerical study of a class of TVD schemes for compressible mixing layers. NASA TM 102194

Schmidt, H. and Schumann, U. 1989. Coherent structure of the convective boundary layer derived from large-eddy simulations. *J. Fluid Mech.*, **200**, 511–562

Scotti, A., Meneveau, C. and Lilly, D. 1993. Generalized Smagorinsky model for anisotropic grids. *Phys. Fluids A*, **5**, 2306–2308

Shyy, W. 1985. A study of finite difference approximations to steady-state, convection-dominated flow problems. *J. Comp. Physics*, **57**, 415–438

Smagorinsky, J. 1963. General circulation experiments with the primitive equations, I. The basic experiment. *Monthly Weather Rev.*, **91**, 99–164

Su, M. and Friedrich, R. 1994. Numerical simulation of fully developed flow in a curved channel. *Int. J. Heat Mass Transfer*, **37**, 1257–1268

Tennekes, H. and Lumley, J. 1972. *A First Course in Turbulence*, 15th ed., MIT, London, UK

van der Ven, H. 1995. A family of large-eddy simulation (LES) filters with nonuniform filter widths. *Phys. Fluids*, **7**, 1171–1172